



Effect of Grain Boundary Engineering on the Work Hardening Behavior of AL6XN Super-Austenitic Stainless Steel

X. J. Guan^{1,3} · Z. P. Jia^{1,3} · M. A. Nozzari Varkani^{1,3} · X. W. Li^{1,2}

Received: 18 June 2022 / Revised: 3 September 2022 / Accepted: 6 September 2022 / Published online: 7 December 2022
© The Chinese Society for Metals (CSM) and Springer-Verlag GmbH Germany, part of Springer Nature 2022

Abstract

To examine the influence of grain boundary engineering (GBE) on the work hardening behavior, the tensile tests were carried out on the non-GBE and GBE AL6XN super-austenitic stainless steel (ASS) samples with a comparable grain size at two strain rates of 10^{-2} s^{-1} and 10^{-4} s^{-1} . The evolution of deformation microstructures was revealed by transmission electron microscopy (TEM) and quasi-in situ electron backscatter diffraction (EBSD) observations. The results show that the influence of GBE on the mechanical properties of AL6XN super-ASS is mainly manifested in the change of work hardening behavior. At the early stage of plastic deformation, GBE samples show a slightly lowered work hardening rate, since the special grain boundaries (SBs) of a high fraction induce a higher dislocation free path and a weaker back stress; however, with increasing plastic deformation amount, the work hardening rate of GBE samples gradually surpasses that of non-GBE samples due to the better capacity of maintainable work hardening that is profited from the inhibited dislocation annihilation by SBs. In a word, the enhanced capacity of sustained work hardening effectively postpones the appearance of necking point and thus efficaciously ameliorates the ductility of GBE samples under the premise of little changes in yield strength and ultimate tensile strength.

Keywords AL6XN super-austenitic stainless steel · Grain boundary engineering · Work hardening behavior · Quasi-in situ observation · Ductility

1 Introduction

It is universally acknowledged that material researchers have never stopped pursuing the excellent strength-ductility match in structural metallic materials. For the vast majority of metals, the improvement of strength is frequently accomplished at the cost of ductility, which is also regarded as the trade-off of strength and ductility [1–4]. For instance, Liu

et al. [5] obtained Cu and Cu alloys with super-refined grains through large deformation followed by a suitable annealing treatment, which significantly improved the strength of these alloys but resulted in a decrease in ductility. He et al. [6] reported that the addition of Al into FeCoNiCrMn high-entropy alloy could visually improve the strength, while it also caused an obvious reduction in ductility. In addition, Qu et al. [7, 8] showed that the strength of Cu-Al alloy and AISI 304L austenitic stainless steel (ASS) could also be notably improved by an equal-channel angular pressing (ECAP) treatment, with a serious loss of ductility. Anyhow, the conventional methods to strengthen metallic materials (e.g., fine grain strengthening, solid solution strengthening and strain strengthening) will potentially cause the decline of ductility. According to the criterion of fracture instability, the significant decline of ductility is mainly caused by a serious loss of work hardening ability. Therefore, how to maintain the work hardening capacity of metallic materials during continued deformation is an important premise for achieving an excellent strength-ductility match.

Available online at <http://link.springer.com/journal/40195>.

✉ X. W. Li
xwli@mail.neu.edu.cn

¹ Department of Materials Physics and Chemistry, School of Materials Science and Engineering, Northeastern University, Shenyang 110819, China

² State Key Laboratory of Rolling and Automation, Northeastern University, Shenyang 110819, China

³ Key Laboratory for Anisotropy and Texture of Materials, Ministry of Education, Northeastern University, Shenyang 110819, China

Many existing studies [9–11] have confirmed that the work hardening of metallic materials is mainly originated from some classical microscopic deformation behaviors such as dislocation multiplication [9], deformation twinning [10], and phase transformation [11]. Obviously, these microscopic deformation behaviors are often related to grain boundaries (GBs) in polycrystalline materials. Therefore, optimizing the amount, distribution or type of GBs in metallic materials should be an effective route to improve their work hardening capacity and consequently strength-ductility match. A recent work by Zhuo et al. [12] suggested that the optimization of grain boundary character distribution (GBCD), also regarded as grain boundary engineering (GBE), can improve the ductility of 316L ASS to some extent without losing strength. More recently, our work [13] on the Cu-16at.%Al alloy further indicated that GBE can effectively improve the high-temperature deformation stability and resistance to GB cracking in face-centered cubic (FCC) metals, and thus significantly ameliorate the strength-ductility match at high temperature. In addition, some other previous works [14–16] have also demonstrated that GBE can effectively improve the deformation uniformity during fatigue process and the resistance to GB cracking during stress corrosion cracking (SCC) process in metallic materials. However, there is as yet no unequivocal knowledge about the specific influence of GBE on the work hardening behavior of materials, which is closely related to their strength-ductility synergy.

Therefore, a commercial AL6XN super-ASS is selected as the target material in the present work, and uniaxially tensile tests are conducted on the GBE and non-GBE samples to explore the influence of GBE on the work hardening behavior of ASS and thus to provide a novel guideline for the design of FCC metallic materials with a good strength-ductility match.

2 Experimental

The AL6XN super-ASS sheets used in the present work were supplied by China Baosteel Co., Ltd. The chemical composition is listed in Table 1. Several as-received materials were directly annealed at 1323 K for 1 h (hereafter abbreviated as 1323 K/1 h) to obtain non-GBE samples with a homogeneous microstructure. In order to get the GBE sample with a comparable grain size to the non-GBE sample, the initial grain size must be lowered before the GBE treatment. Therefore, other as-received materials underwent firstly a process of grain refinement (base material, BM), followed by a series

of thermo-mechanical processes (TMPs). Specifically, four samples obtained from the grain-refined sheet by wire electrical discharge machining (WEDM) were firstly subjected to a cold rolling with a small reduction of 5%, and subsequently annealed at 1323 K for different time of 10 min, 12 h, 18 h and 24 h (abbreviated as R5-10 m, R5-12 h, R5-18 h and R5-24 h), respectively. Thereinto, the grain refinement is achieved by cold rolling with a large deformation (40%) and annealing at 1323 K/10 min. It is worth mentioning that, in the above process, all samples were cooled by water quenching after annealing.

Electron backscatter diffraction (EBSD) observations were applied to analyze the microstructures of non-GBE and TMPed samples by using a JEOL JSM 7001F field emission scanning electron microscope (FESEM) equipped with an orientation imaging microscopy (OIM) system. EBSD samples were prepared by a standard method including mechanically grinding and electrolytic polishing in a solution of $\text{HClO}_4:\text{CH}_3\text{COOH} = 1:9$ (vol.) at 40 V for 30 s to obtain a smooth stress-free surface. The main operation conditions for EBSD observation involve 30 kV accelerating voltage, 14 nA current and 70° beam incidence angle. At least three different regions (each region with an area of $900 \times 1200 \mu\text{m}^2$) on each sample were measured with a step of $1 \sim 2 \mu\text{m}$ to ensure the reliability of statistics. The coincidence site lattice (CSL) boundaries were identified according to the Brandon criterion of $\Delta\theta \leq 15^\circ \Sigma^{-1/2}$. CSL boundaries with $3 \leq \Sigma \leq 29$ were defined as low-energy special boundaries (SBs), whereas other high angle GBs were judged as random high angle grain boundaries (RHAGBs) [17]. The fraction of each type of SBs was defined as the ratio of its length to the length of entire GBs. Grain sizes (annealing twins included) were assessed from the EBSD data by employing automated mean linear intercept (MLI) measurements.

The tensile samples with a gauge dimension of $16 \text{ mm} \times 4 \text{ mm} \times 2 \text{ mm}$ and a total length of 53.4 mm were prepared from the non-GBE and GBE samples by WEDM (long axis parallel to rolling direction). Then, in order to conveniently perform quasi-in situ EBSD observations on tensioned samples, all samples were subjected to mechanical grinding and electropolishing to obtain stress-free and smooth surface. It is important to note that, for quasi-in situ observations, indentation positioning method was applied to mark the region for EBSD observations. Specifically, before the tensile test, a triangular mark was engraved on the observing surface of the sample by a microhardness tester and the EBSD observation was conducted near the marked region. Then, the marked non-GBE and GBE samples were

Table 1 Chemical composition (wt%) of AL6XN super-ASS used in the present study

| C | Si | Mn | P | S | N | Cr | Mo | Ni | Cu | Fe |
|-------|-------|-------|-------|-------|-------|------|------|------|-------|------|
| 0.012 | 0.302 | 0.343 | 0.001 | 0.002 | 0.188 | 18.2 | 5.56 | 22.7 | 0.554 | Bal. |

tensioned to a true strain of 10% at a strain rate of 10^{-4} s^{-1} . Subsequently, the EBSD observation was performed again on the same region recorded already by indentation. Finally, repeat the last two steps to complete quasi-in situ observations at a true strain of 20%.

The tensile tests up to true strains of 10% and 20% and to fracture were carried out at room temperature and strain rates of 10^{-2} s^{-1} and 10^{-4} s^{-1} using an AG-X Plus 100 kN microcomputer-controlled electronic universal testing machine. Transmission electron microscopy (TEM) observations were applied on the sample tensioned to the true strains of 10% and 20% using an FEI Tecnai G²20 transmission electron microscope operated at 200 kV. All TEM samples were firstly ground from the original thickness of 500 μm to $\sim 50 \mu\text{m}$ by emery papers from #600 to #2000, followed by a two-jet electropolishing in a solution of $\text{HClO}_4:\text{CH}_3\text{COOH} = 1:19$ (vol.) with a voltage of 18 V at room temperature.

3 Results

3.1 Evolution of GBCD with Annealing Time

The reconstructed GBCD images for the BM and the TMPed specimens are displayed in Fig. 1, where different types of GBs are characterized by the lines with different colors, namely red, green, blue and yellow lines represent $\Sigma 3$, $\Sigma 9$, $\Sigma 27$ and other low Σ CSL GBs, respectively. The RHAGBs are represented by black lines. Obviously, with the increase in annealing time, the grain size of TMPed samples increases visually. Moreover, compared with the BM sample, the fractions of SBs (f_{SBs}) in TMPed samples are improved to varying degrees, and correspondingly, the connectivity of the RHAGB network in different TMPed samples is interrupted to different extents. For instance, the SBs, mainly including annealing twin boundaries (TBs), induced by TMP effectively block the connection of RHAGBs, as illustrated by the black arrows in Fig. 1c, d.

To accurately evaluate the degree of GBCD optimization of TMPed samples, some GBE-quantifying parameters including the f_{SBs} , the ratio ν and the value $f_{\text{J2}}/(1-f_{\text{J3}})$ are analyzed, as shown in Fig. 2. Among these GBE-quantifying parameters, the ratio ν is the ratio of twin-related domain (TRD) size to grain size, which reflects the nucleation degree of annealing twins during the TMP [18]. The TRD is actually a grain-cluster, in which grains are connected with each other by $\Sigma 3^n$ ($n = 1, 2, 3$) SBs, namely there exists a twinning relation between neighboring grains in one TRD. In a certain TRD, the higher the twinning level, the higher the fraction of $\Sigma 3^n$ SBs is. The value $f_{\text{J2}}/(1-f_{\text{J3}})$ reflects the degree of RHAGB network connectivity blocked by SBs [19], where the f_{J2} and f_{J3} represent the proportion of J2

triple junctions with two SBs and J3 triple junctions with three SBs, respectively. Among the triple-junctions of J0, J1, J2, and J3, the RHAGBs are interconnected with each other at the J0 and J1 junctions, and thereby cracks can pass through the junctions without hindrance and propagate along the RHAGBs. Besides, J3 junctions are generally too stable to meet the condition for crack nucleation and propagation. Hence, only at the J2 junctions can the cracks be captured by SBs. For this reason, the capture probability of cracks is quantified by statistically calculating the distribution of $f_{\text{J2}}/(1-f_{\text{J3}})$. Obviously, with the extension of annealing time, all the GBE-quantifying parameters of TMPed samples gradually increase until 18 h and then decrease. Such a unique variation trend should be attributed to the distinctive evolution behavior of TRD at different annealing stages [18, 20]. Specifically, as the annealing time is less than 18 h, the microstructure evolution is mainly manifested by the growth of TRD and the nucleation of annealing twins; however, as the annealing time exceeds 18 h, de-twinning phenomenon occurs in TRDs [21], which lowers the ratio ν and thus induces the decreases in f_{SBs} and $f_{\text{J2}}/(1-f_{\text{J3}})$ [18].

According to the analyses of the above signifying parameters for GBE evaluation, we chose the TMPed sample (R5-18 h) treated by 5% cold rolling and 1323 K/18 h annealing as the GBE sample for a comparison with the non-GBE sample, as shown in Fig. 3. Clearly, the initial microstructures of these two samples consist of essentially equiaxed grains with random orientations, and the average grain sizes (annealing twins included) of the non-GBE and GBE samples are fairly comparable, i.e., 28.0 μm for non-GBE and 30.6 μm for GBE samples (Fig. 3a, d). Therefore, the influence of grain size and texture on the mechanical properties can be basically ruled out. In addition, the GBE-quantifying parameters of GBE sample are obviously higher than those of non-GBE sample. For example, the f_{SBs} and the ratio ν increase from 46.1% to 75%, and from 2.0 to 5.2 after GBE treatment, respectively. Besides, the parameter $f_{\text{J2}}/(1-f_{\text{J3}})$ increases from 0.11 to 0.35. Accordingly, the connectivity of RHAGBs is indeed effectively weakened by the GBE treatment, as representatively indicated by arrows in Fig. 3b, c, e, f.

3.2 Influences of GBE on Mechanical Properties

Figure 4 shows the comparisons of the tensile engineering stress–strain curves, the true stress–strain curves and strain hardening rate curves for the non-GBE and GBE samples tensioned at different strain rates of 10^{-2} s^{-1} and 10^{-4} s^{-1} . Obviously, the yield strength of GBE samples is roughly equal to those of non-GBE samples either at the higher strain rate of 10^{-2} s^{-1} or lower strain rate of 10^{-4} s^{-1} (Fig. 4a, b). At the higher strain rate, the ultimate tensile strength of GBE sample is slightly lower than that of non-GBE sample, but the difference becomes subtle at the lower strain rate

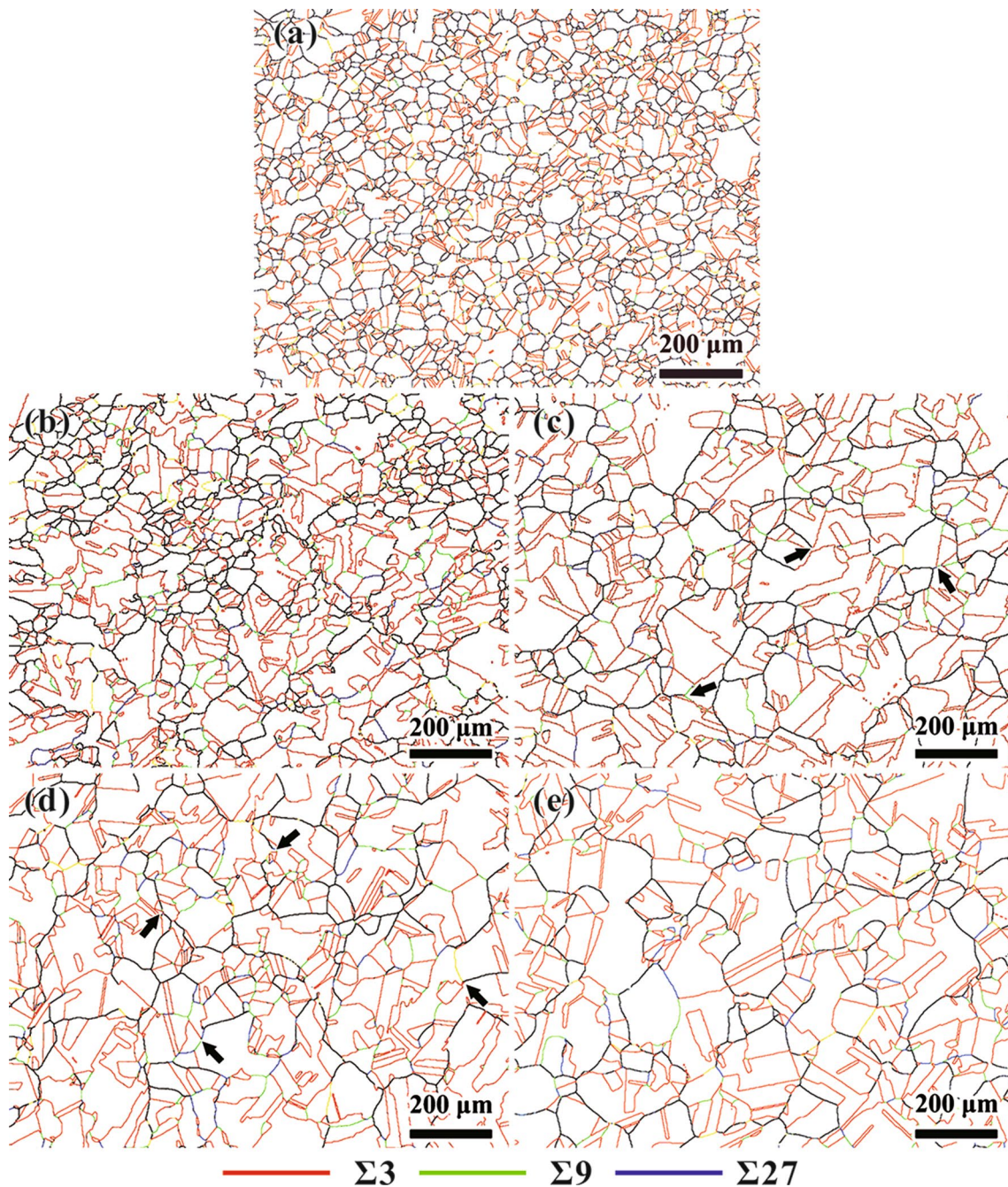


Fig. 1 GBCD of BM **a** and TMPed **b-e** samples with different annealing time of 10 min **b**, 12 h **c**, 18 h **d**, 24 h **e**

(Fig. 4a, b). In addition, the ductility of GBE samples is superior to that of non-GBE samples, especially at the lower strain rate, as shown in Fig. 4a, b. Such a unique difference in the tensile performance of GBE and non-GBE samples must be closely related to the influence of GBE on the work hardening behavior at different strain rates [4].

Similar to most planar slip alloys, the work hardening rate curves of AL6XN super-ASS exhibit a multi-stage characteristic at different strain rates [4, 22], which are labeled as

I, II, III and IV, respectively, as indicated in Fig. 4c, d. At the early stage of deformation (Stage I), the work hardening rates of both non-GBE and GBE samples decrease sharply, due to the occurrence of plastic deformation. Subsequently, an obvious upswing phenomenon of work hardening rate appears in the both samples at the Stage II. Some previous work [4, 23, 24] suggested that the typical behavior of work hardening rate upswing should be ascribed to the enhanced dislocation slip planarity caused by low stacking fault energy

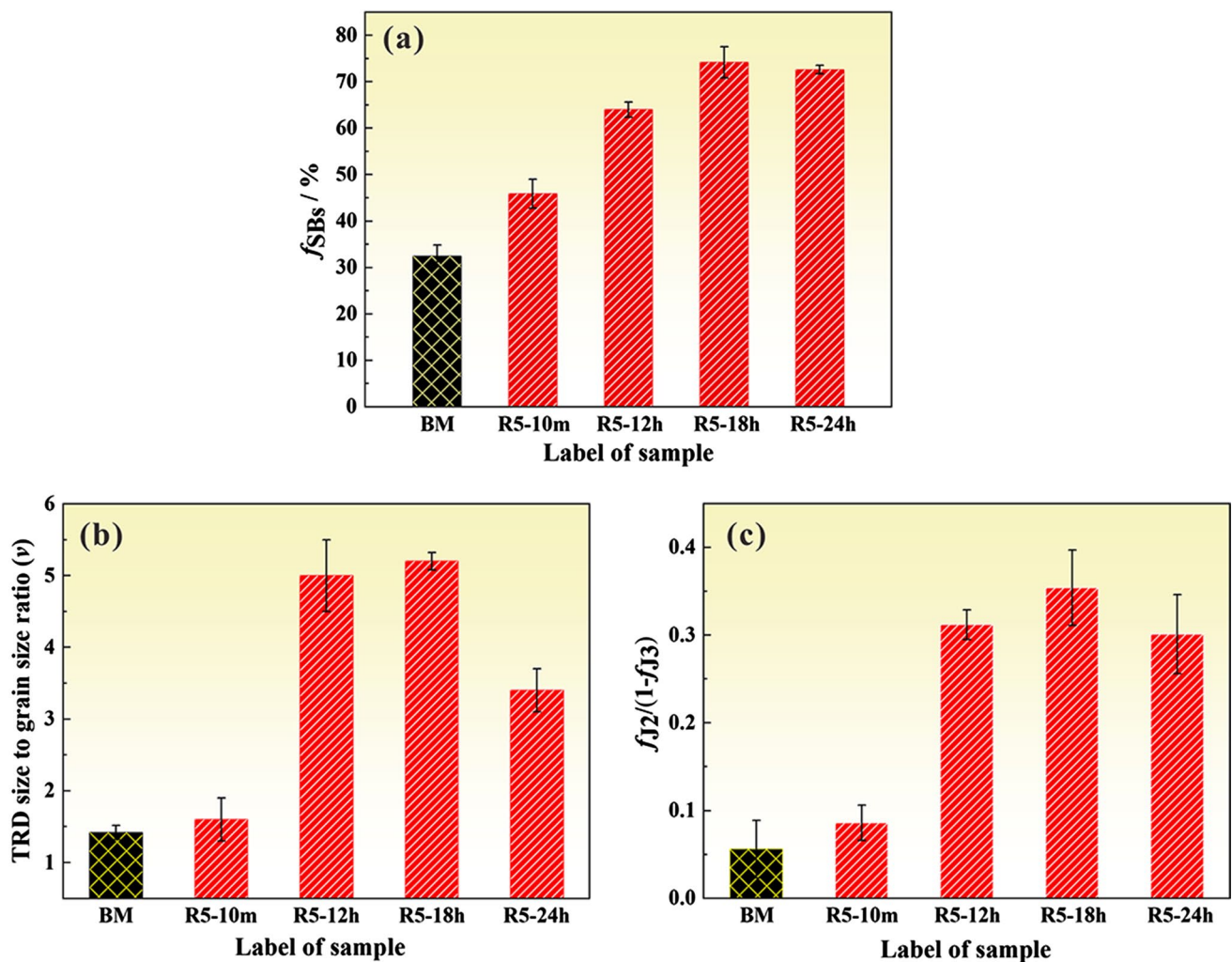


Fig. 2 Comparisons of the fraction of SBs (f_{SBs}) **a**, ratio (v) of TRD size to grain size **b** and $f_{J2}/(1-f_{J3})$ **c** in BM and TMPed samples. Note that, the f_{J2} and f_{J3} in **c** refer to the fraction of J2 and J3 junctions, respectively

or short-range order (SRO) structures, which effectively reduces the free path of dislocation slip and successfully weakens the dislocation recovery behavior. Afterward, the work hardening rates of both non-GBE and GBE samples enter into continuous decline stages. Especially, the decline rate for the Stage III and Stage IV is obviously different, and it is significantly lower in the Stage III rather than Stage IV. In addition, in the first three stages I-III (true strain < 20%), the work hardening rate curves of GBE samples are always lower than those of non-GBE samples; however, it becomes reversed at the end of Stage III, since the work hardening rate of GBE samples keeps essentially unchanged in Stage III, as displayed in Fig. 4c, d. In the final stage of tensile deformation (Stage IV), the ability of sustained work hardening of GBE samples is, to some extent, better than that of non-GBE samples, so that the work hardening rate of GBE samples exceeds that of non-GBE sample, thus delaying the occurrence of necking point and improving the ductility

of AL6XN super-ASS, as indicated by the blue arrows in Fig. 4c, d.

3.3 Quasi-in situ Observations of Deformation Behavior in Non-GBE and GBE Samples

To deeply understand the influence of GBE on the work hardening behavior of AL6XN super-ASS, quasi-in situ EBSD observations were performed on non-GBE and GBE samples, respectively.

Figure 5 shows the reconstructed inverse pole figure (IPF), GBCD and Kernel average misorientation (KAM) maps in the same spatial location of a single non-GBE sample tensioned to different true strain amounts of 0, 10% and 20%. From the IPF maps, it can be easily learned that the color of some grains changes in various ways as the true strain increases, indicating that the lattice of some surface grains is rotated to different orientations [25]. For instance,

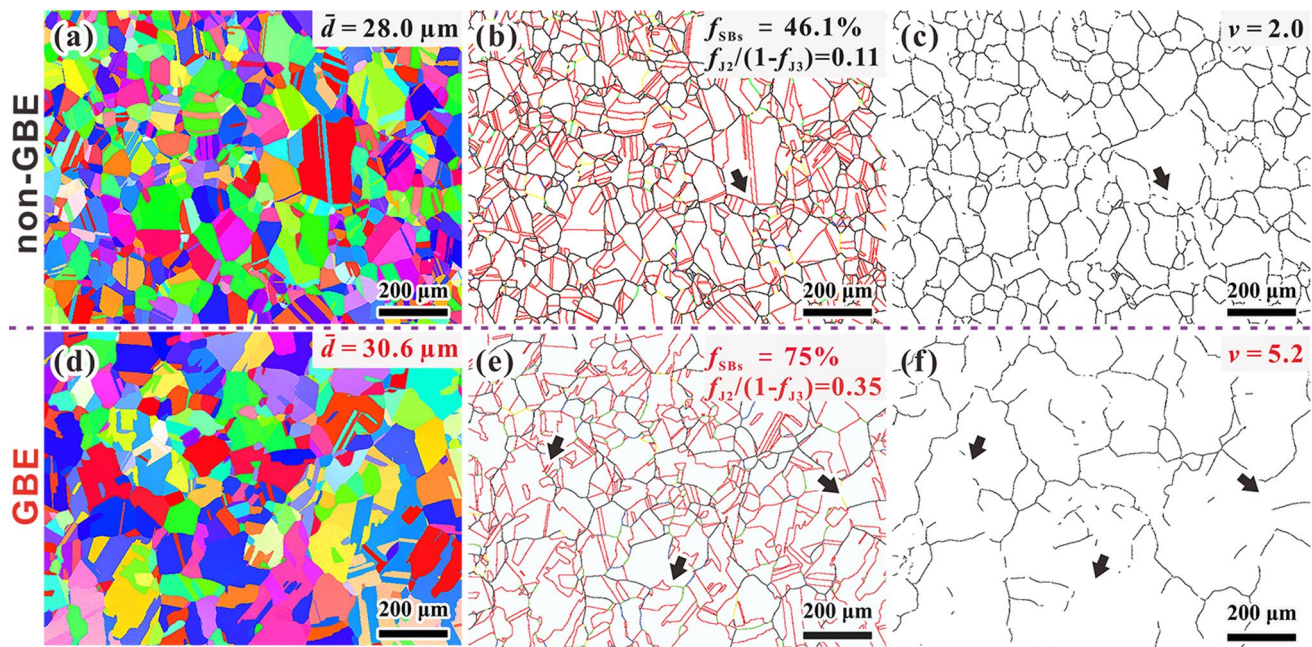


Fig. 3 Inverse pole figure (IPF) maps **a, d**, GBCD **b, e** and corresponding RHAGB network maps **c, f** of non-GBE **a-c** and GBE **d-f** samples

the color of some grains gradually turns into green as they rotate toward $\langle 101 \rangle$, as shown by the black arrows in Fig. 5a, b, c. The grain rotation will not only induce an obvious tensile texture in the non-GBE sample (Fig. 5c), but also alter the orientation relations between adjacent grains. Figure 5a'–c' intuitively shows the evolution of GBCD in non-GBE sample with the increase in true strain. Obviously, some SBs lose their specificity due to the transformation of grain orientation relationship on both sides of GBs, as shown by the black arrows in Fig. 5a'–c'.

In EBSD observation, KAM can be calculated for the grains by averaging the misorientation among the point at a center of the Kernel to its nearest neighbors [25–27]. When the plastic deformation among subregions in a grain is homogeneous, a low KAM value (angle) will be obtained; conversely, a large deformation inhomogeneity will consequently induce a large KAM. Therefore, KAM is commonly used as a tool in OIM analysis to qualitatively evaluate local strain distribution and dislocation density [28]. Moreover, some previous studies have also confirmed that the distribution of KAM values highly coincides with the distribution of geometrically necessary dislocations (GNDs) [29–31], which can effectively represent the deformation uniformity of polycrystalline materials [32]. In general, KAM is low in recrystallized grains but high in deformed grains. The variation in KAM of the non-GBE sample is intuitively presented in Fig. 5a''–c''. Clearly, in the reconstructed KAM maps, the KAM of undeformed and fully recrystallized non-GBE samples is predictably low (Fig. 5a''). With increasing deformation amount, the KAM of the sample gradually

becomes larger (Fig. 5a''–c''). Moreover, comparing the GBCD (Fig. 5a'–c') and KAM maps (Fig. 5a''–c''), it can be observed that the regions with high local misorientations are mainly concentrated on both sides of RHAGB after deformation (Fig. 5b', c'), indicating an obvious strain concentration that occurs at RHAGB.

The IPF, GBCD and KAM maps in the same spatial location of a single GBE sample tensioned to different true strain amounts of 0, 10% and 20% are also reconstructed according to the quasi-in situ EBSD observation, as shown in Fig. 6. Similar to the case in non-GBE samples, a significant grain rotation behavior was also observed in GBE samples (see black arrows in Fig. 6a–c), which also causes some local transition from SBs to RHAGB (see the black arrows in Fig. 6a'–c'); however, the stronger texture occurring in non-GBE sample does not form in the GBE sample (Fig. 6c). More importantly, the distribution of KAM in the GBE sample is more uniform, as contrastively shown in Fig. 5a''–c'' and Fig. 6a''–c''. Specifically, at the true strain of 10%, a significant increase in KAM has been observed at RHAGBs in non-GBE samples (Fig. 5b', b''), but not in GBE samples (Fig. 6b', b''). Moreover, the difference of KAM distribution between these two samples becomes more obvious with increasing strain amount, as shown in Fig. 5b'', c'' and Fig. 6b'', c''. For demonstrating it more straightforwardly, the distribution comparisons of KAM values versus the relative frequency are provided in Fig. 7. By comparing the relative frequency at the two strains of 10% and 20%, it can be seen that the peak values of the GBE sample are lower than those of the non-GBE sample, which also indicates a

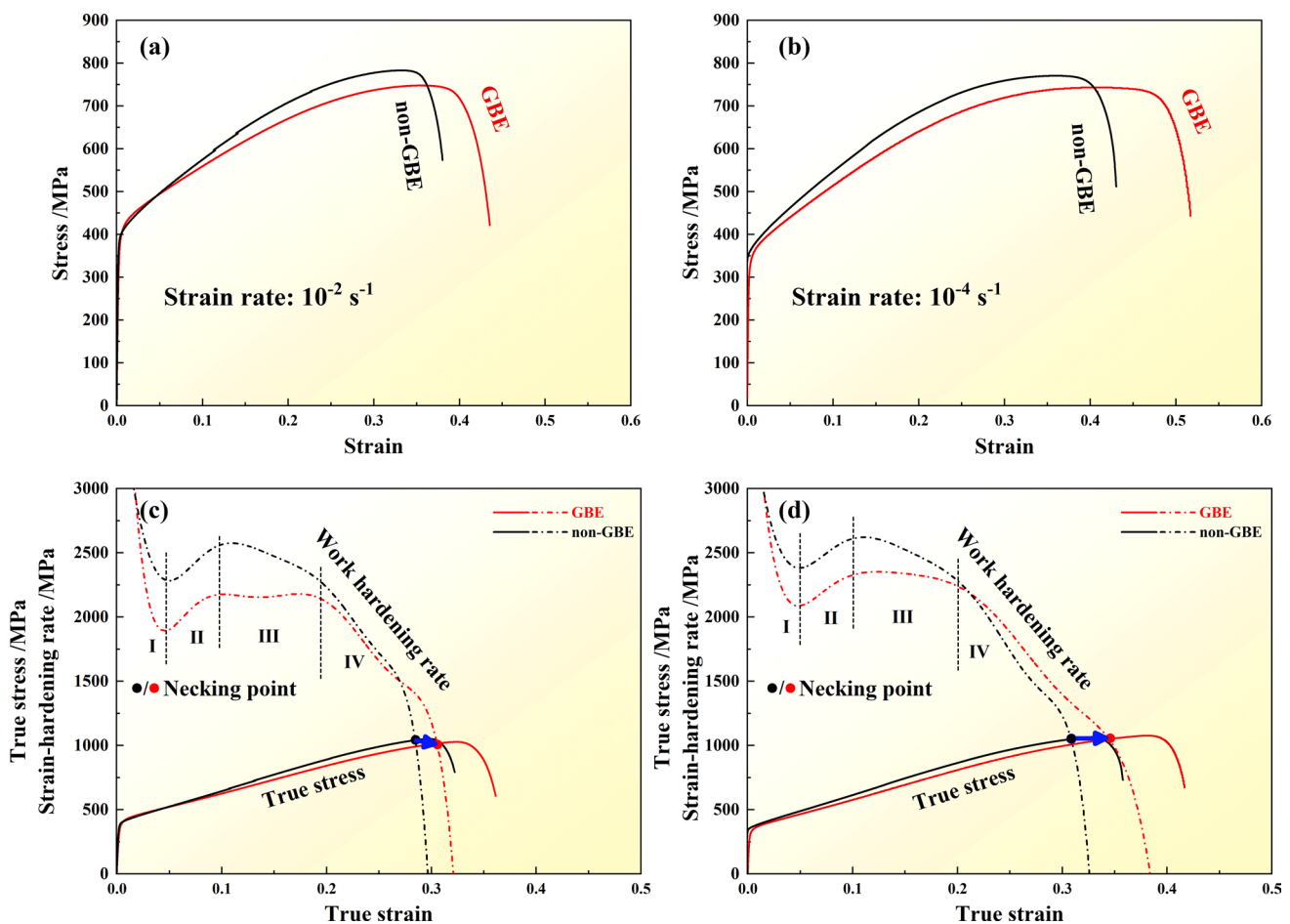


Fig. 4 Comparisons of tensile properties **a, b** and work hardening rate **c, d** of non-GBE and GBE samples at different strain rates of 10^{-2} s^{-1} **a, c** and 10^{-4} s^{-1} **b, d**

more uniform strain distribution in the GBE sample [12]. Our previous studies [14, 20] have suggested that the difference is mainly related to the deformability of the high f_{SBs} . For instance, KAM does not significantly increase near SBs in both GBE and non-GBE samples, as illustrated by the red arrows (taking the annealing TBs with the highest proportion as an example) in Fig. 5b', c', b'', c'' and Fig. 6b', c', b'', c''. Besides, some other studies [33–35] also indicated that a higher back stress might exist in the areas with higher KAM. Therefore, the GBE treatment not only effectively improves the deformation uniformity, but also reduces the back stress near RHAGBs to a certain extent, and thus inevitably influences the work hardening behavior of AL6XN super-ASS.

3.4 Evolution of Deformation Microstructures in Non-GBE and GBE Samples

To further understand the effect of GBE on the deformation behavior of AL6XN super-ASS, TEM observations were

also conducted on the non-GBE and GBE samples tensioned to true strains of 10% and 20% at strain rates of 10^{-2} s^{-1} and 10^{-4} s^{-1} .

Figure 8 shows the deformation microstructures of non-GBE and GBE samples tensioned to true strains of 10% and 20% at a high strain rate of 10^{-2} s^{-1} . At the true strain of 10%, the deformation microstructures of these two samples are dominated by planar slip dislocation structures; however, the interactions between dislocations and different GBs are widely divergent. Specifically, the slipping of dislocations is significantly hindered at the RHAGBs in the non-GBE sample but not at the SBs in the GBE sample, as compared in Fig. 8a, b. It is chiefly because the interface of SBs can be bypassed by dislocations through decomposition or slip transmission [36–38]. Certainly, the weakened dislocation pile-up behavior is beneficial to the deformation uniformity of GBEed materials; however, it also reduces the hindrance of interface on dislocation motion, which will significantly influence the back stress and even work hardening behavior. As the true strain reaches 20%, the pile-up of planar slip

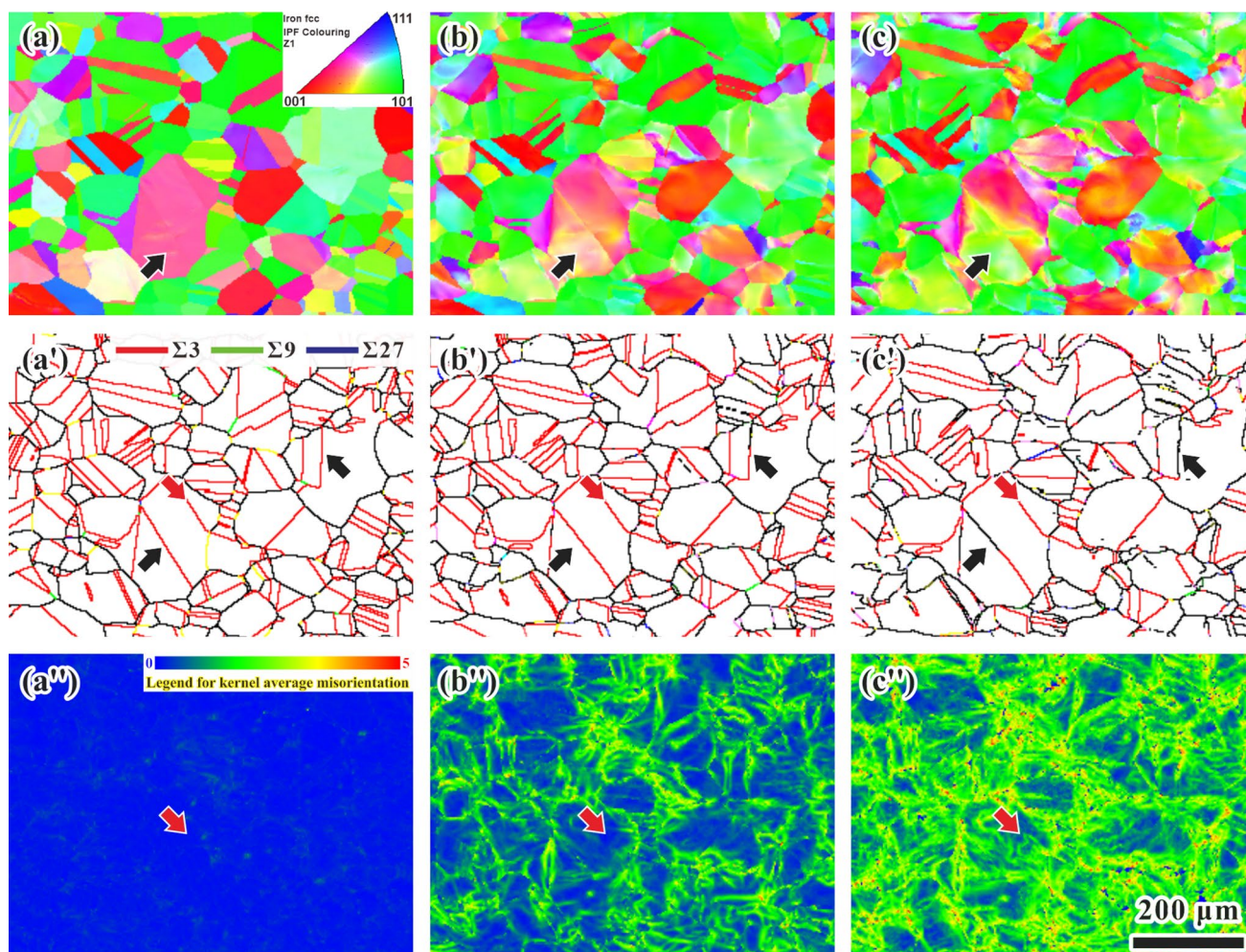


Fig. 5 The quasi-in situ sequential IPF colored EBSD **a-c**, GBCD **a'-c'** and KAM distribution **a''-c''** maps in the same spatial location of a single non-GBE sample undeformed **a, a', a''** and subsequently tensioned to different true strains of 10% **b, b', b''** and 20% **c, c', c''** at a strain rate of 10^{-4} s^{-1}

dislocation structure at RHAGBs in the non-GBE sample becomes more serious and even induces few deformation twins to form nearby (Fig. 8c). In addition, a large number of dislocation cell structures with small size appear together at the RHAGBs in the non-GBE sample, indicating that the dislocation recovery has happened in the non-GBE sample to some extent [39]; however, no obvious dislocation recovery occurs at SBs in the GBE sample (Fig. 8d). Therefore, it can be learnt that the high f_{SBs} introduced by GBE has an inhibitive effect on the occurrence of dislocation recovery at RHAGBs.

Figure 9 shows the deformation microstructures of non-GBE and GBE samples tensioned to true strains of 10% and 20% at a low strain rate of 10^{-4} s^{-1} . Compared with the case at a high strain rate of 10^{-2} s^{-1} , the slip mode of dislocations at the low strain rate is still mainly featured by planar slip; however, the wavy slip, especially at RHAGBs in non-GBE samples, cannot be ignored. Specifically, at the

true strain of 10%, some dislocation cells have appeared near the RHAGBs in the non-GBE sample (Fig. 9a) and become more obvious with increasing true strain amount to 20% (Fig. 9c). Here, the operation of more obvious wavy slip near RHAGBs of non-GBE samples can be understood from the following two aspects: (1) In AL6XN super-ASS, the planar slip of dislocations is mainly caused by the so-called slip plane softening effect resulting from cutting of the SRO structures by moving dislocations [4, 39]. At a low strain rate, the dislocation velocity is relatively low, which induces an increased opportunity of dislocations to bypass the SRO structures by cross-slip, thus weakening the slip plane softening effect. (2) The more notable strain concentration near RHAGBs exacerbates the consumption of SRO structures to a certain extent [40], which further weakens the slip plane softening effect. The similar results were also reported in the previous work by Leverant et al. [41]. On the contrary, the dislocation arrangement near SBs (taking the

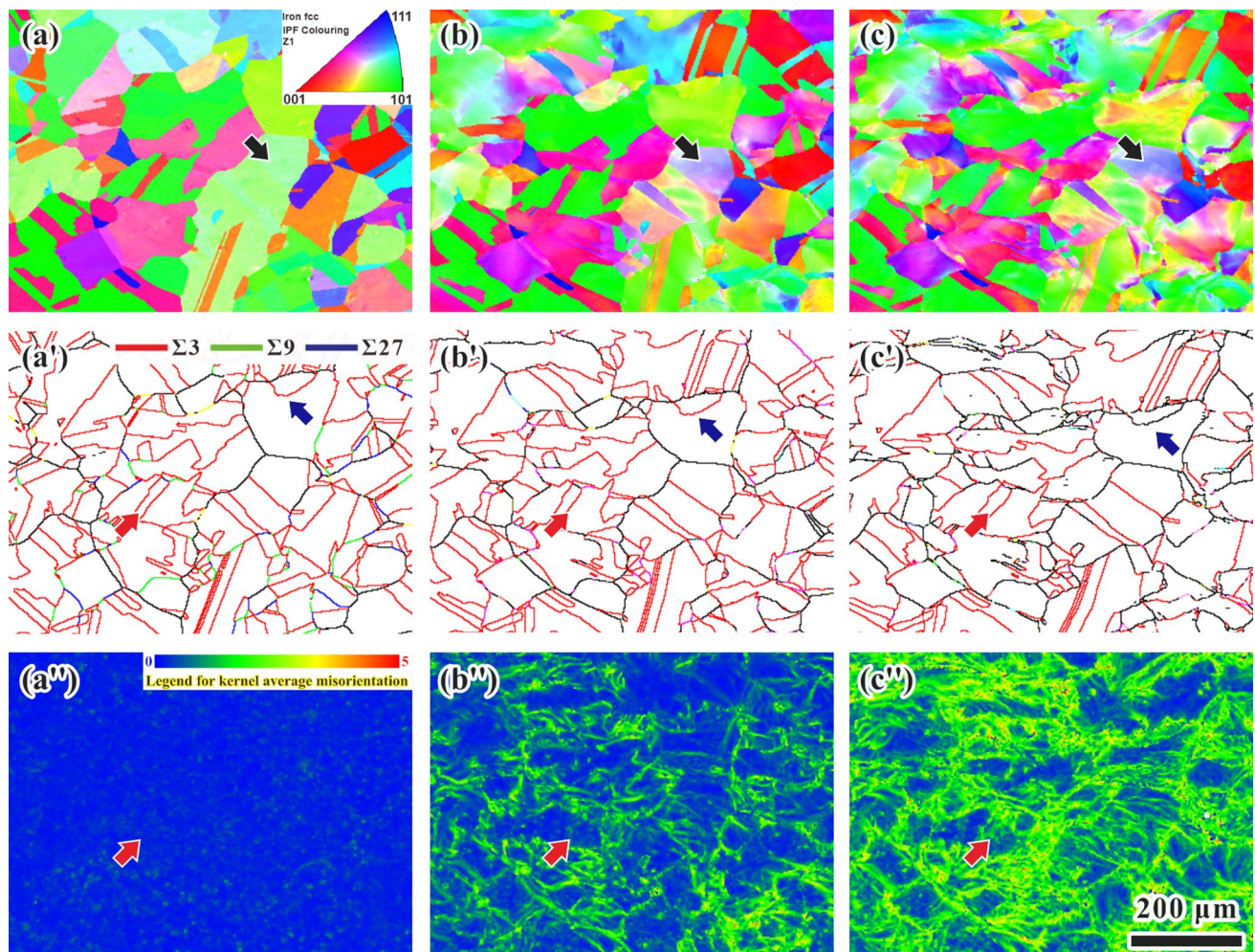


Fig. 6 The quasi-in situ sequential IPF colored EBSD **a-c**, GBCD **a'-c'** and KAM distribution **a''-c''** maps in the same spatial location of a single GBE sample undeformed **a, a', a''** and subsequently tensioned to different true strains of 10% **b, b', b''** and 20% **c, c', c''** at a strain rate of 10^{-4} s^{-1}

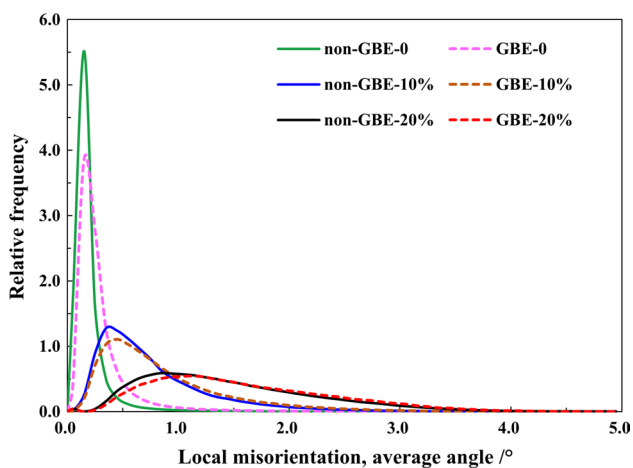


Fig. 7 Local misorientation (KAM values) versus relative frequency for the GBE and non-GBE samples tensioned to different true strains of 0, 10% and 20%

TB as an example) in the GBE sample is still dominated by planar slip bands, which does not change significantly with the increase in deformation amount (Fig. 9b, d). Therefore, at the low strain rate, the significant dislocation recovery behavior is more effectively inhibited by the GBE treatment.

4 Discussion

The striking results of the present work show that the GBE treatment has little effect on the yield strength of AL6XN super-ASS, but slightly reduces the tensile strength and improves the ductility to a certain extent. Such an influence of GBE on the mechanical properties of AL6XN super-ASS mainly can be understood in terms of different stages of plastic deformation (Fig. 4c, d).

As aforementioned, the work hardening behavior of metallic materials originates principally from the hindrance

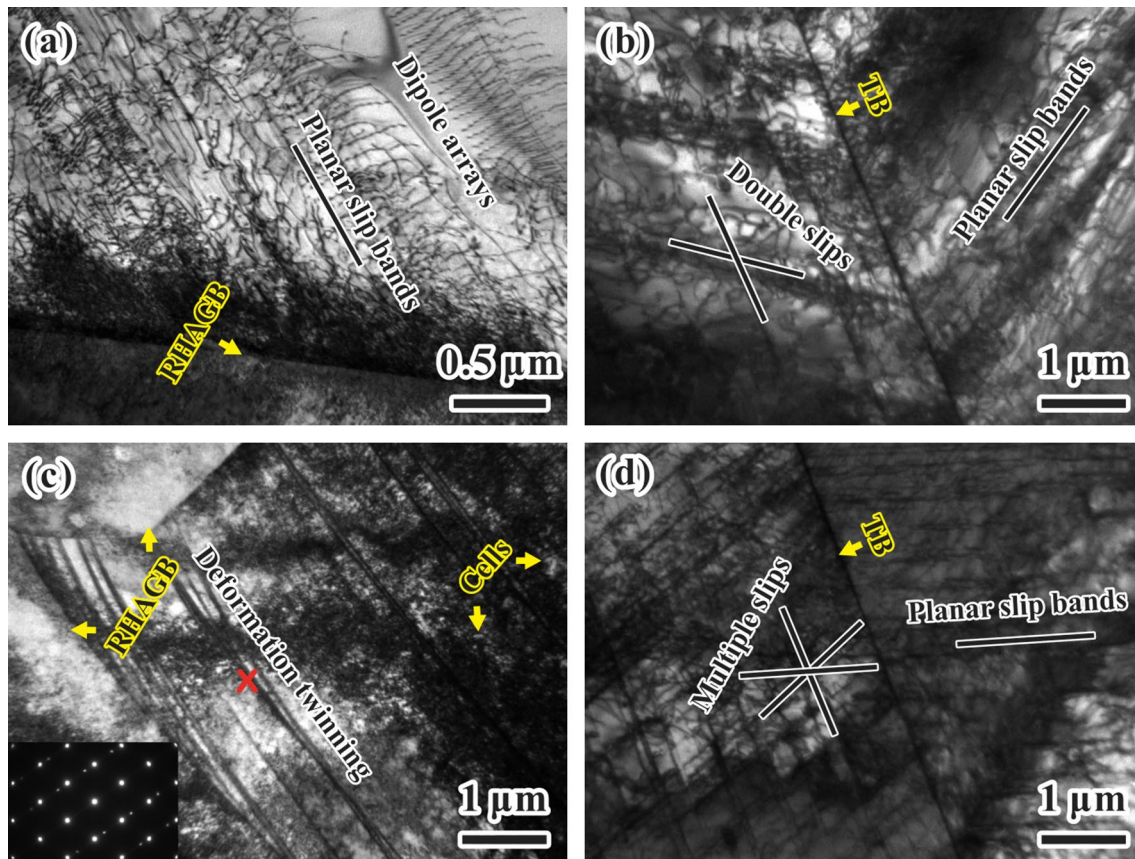


Fig. 8 TEM micrographs showing the deformation microstructures near the RHAGBs of non-GBE samples **a, c** and annealing TBs of GBE samples **b, d** tensioned to different true strains of 10% **a, b** and 20% **c, d** at a high strain rate of 10^{-2} s^{-1}

on the plastic deformation. For AL6XN super-ASS, the plastic deformation behavior is mainly manifested as dislocation slipping and deformation twinning, as shown in Figs. 8 and 9. In the early stage of plastic deformation, the deformation twins are rarely observed in the deformation microstructures except for a small amount near RHAGBs where the stress is obviously concentrated, as shown in Figs. 5c', 8 and 9. In this case, the work hardening contributed by the formation of deformation twins can be almost negligible in AL6XN super-ASS. Therefore, the work hardening of AL6XN super-ASS should be mainly attributed to the dislocation increment and the interaction between dislocations and GBs.

Firstly, the increment of dislocations plays a leading role in the work hardening of AL6XN super-ASS. Certainly, the higher the increment rate of dislocations, the higher the work hardening rate is. According to one-internal-variable Kocks-Mecking model [42], the evolution of total dislocation density (ρ) with true plastic strain (ϵ_p) can be expressed by

$$\frac{d\rho}{d\epsilon} = M \left(\frac{d\rho^+}{d\epsilon_p} - \frac{d\rho^-}{d\epsilon_p} \right), \quad (1)$$

where M is the Taylor factor, $d\rho^-/d\epsilon_p$ is the rate of dislocation annihilation, and $d\rho^+/d\epsilon_p$ is the rate of dislocation storage that is inversely related to the dislocation mean free path (L) [43], namely

$$\frac{d\rho^+}{d\epsilon_p} = \frac{1}{bL}, \quad (2)$$

where b is the Burgers vector. Substituting Eq. (2) into Eq. (1), one obtains

$$\frac{d\rho}{d\epsilon} = M \left(\frac{1}{bL} - \frac{d\rho^-}{d\epsilon_p} \right). \quad (3)$$

At the initial stage of plastic deformation (Stage I), due to the low dislocation density, dislocations are difficult to entangle with each other. In this case, the mean free path L should be as large as the grain size. Therefore, according to Eq. (3), the storage rate of dislocations at the stage is so low, and it can be negligible. In this case, dislocation annihilation dominates the stage, thus leading to the sharp decrease in work hardening rate (Fig. 4c, d).

As the plastic flow further proceeds into Stage II, the dislocation density of AL6XN super-ASS increases

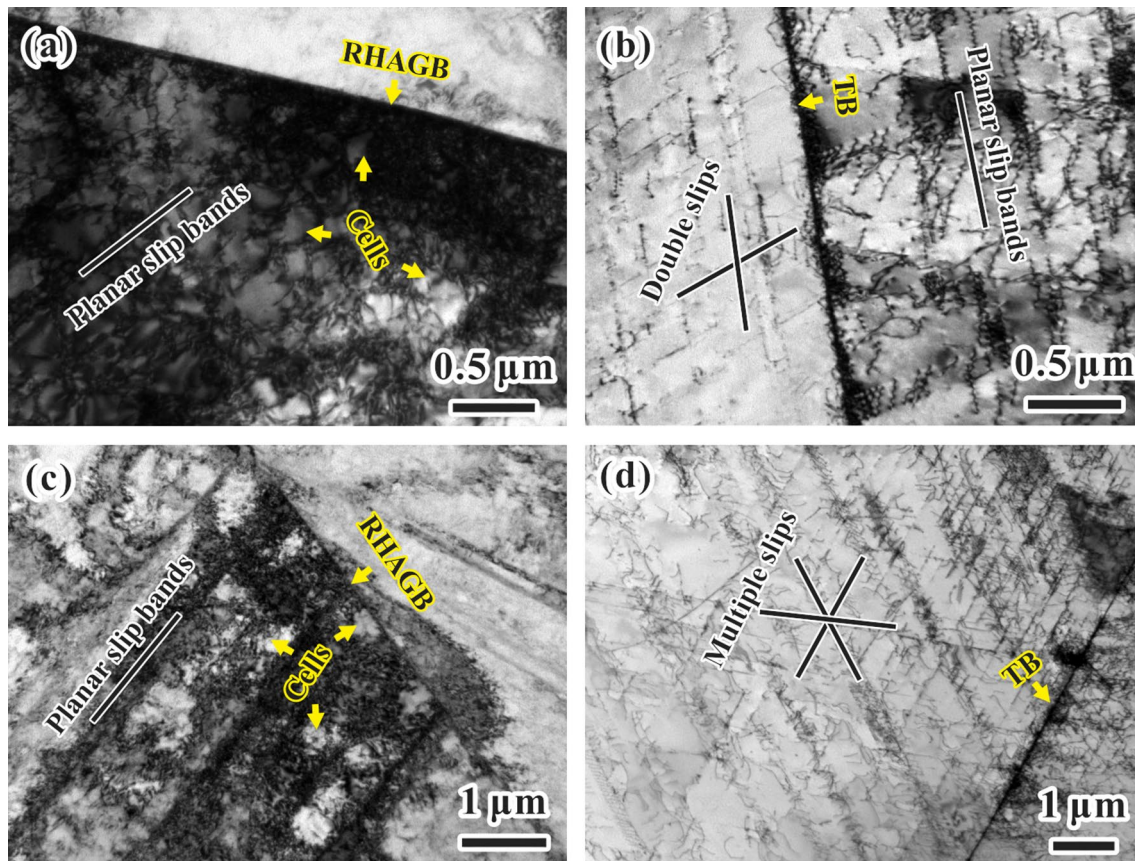


Fig. 9 TEM micrographs showing the deformation microstructures near the RHAGBs of non-GBE samples **a, c** and annealing TBs of GBE samples **b, d** tensioned to different true strains of 10% **a, b** and 20% **c, d** at a low strain rate of 10^{-4} s^{-1}

significantly, which induces a dramatic decrease in the free path of dislocations, and thus obviously increases the rate of dislocation storage. Moreover, the dislocation slip mode governed jointly by SRO and SFE strongly influences the dislocation annihilation at the stage. Owing to the existence of a large number of Cr–N or Mo–N SRO structures [44–46], the dislocation slip mode is dominated by planar slip at the early stage of plastic deformation of AL6XN super-ASS, as shown in Figs. 8a, b and 9a, b. Han et al. [4] suggested that, compared with wavy slip, planar slip of dislocations can not only effectively reduce the mean free path of dislocation slip, but also significantly suppress the annihilation of dislocations. Obviously, both of the aspects are conducive to increasing the increment rate of dislocation density according to Eq. (3). Therefore, a considerable upswing appears in the work hardening rate at Stage II (Fig. 4c, d). It should be emphasized that, in the early stage of plastic deformation, the free path of dislocations in the GBE sample is larger than that in the non-GBE sample, since much more SBs in the GBE sample allow dislocations to slip across them. According to Eq. (3), it is adverse to the increment rate of dislocations

in the GBE sample. In addition, due to the conductivity of SBs on dislocation slipping, the density of GNDs near SBs is significantly lowered (Fig. 6), bringing about the reduction in back stress between grains and the weakness in work hardening rate in the GBE sample [30, 47, 48]. As a result, the work hardening rate of the GBE sample is slightly lower than that of non-GBE sample at the early stage of plastic deformation (Fig. 4c, d).

As the plastic deformation enters into Stage III, the SRO structures are greatly consumed by moving dislocations, and meanwhile, the local stress concentration arises due to the dislocation pile-ups at RHAGBs [40], so that wavy slip of dislocations is locally activated (Figs. 8c and 9c), which apparently increases a possibility for dislocation annihilation. Therefore, the work hardening rate begins to decline slowly at this stage in the non-GBE sample (Fig. 4c, d). In contrast, the dislocation annihilation can be effectively inhibited in the GBE sample, since the SBs of a high fraction effectively alleviate the piling-up behavior of dislocations (Figs. 8b, d and 9b, d), which greatly improves the sustained work hardening ability. Hence, the work hardening rate of GBE samples barely decreases in Stage III (Fig. 4c, d).

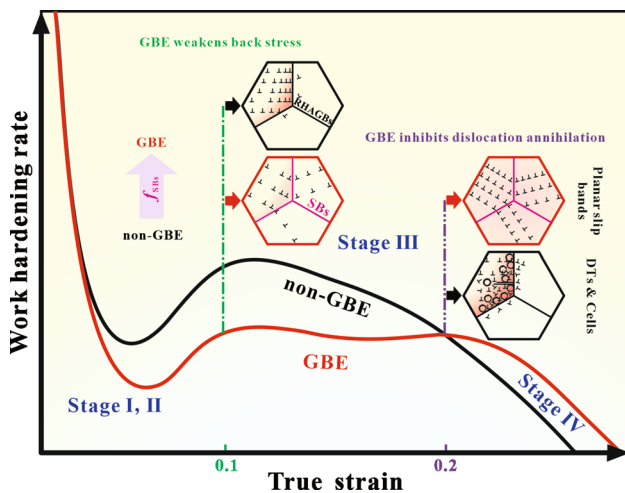


Fig. 10 Schematic diagram showing the mechanism for the influence of GBE on the work hardening rate of AL6XN super-ASS

At the last stage of uniform plastic deformation (Stage IV), the dislocation density in non-GBE and GBE samples reaches a fairly high level. The storage capacity for dislocations is almost close to a saturated state. In this case, the annihilation of dislocations becomes highly remarkable. With the increase in strain, the increasing rate of dislocation density drops sharply, thus inducing a rapid decrease in the work hardening rate in these two samples (Fig. 4c, d). However, the deformation uniformity of GBEed AL6XN super-ASS is effectively improved by high f_{SBs} (Figs. 5c'' and 6c''), which equivalently improves the overall storage capacity of dislocations [49, 50]. Therefore, at the last stage of plastic deformation, the decrease in work hardening rate of the GBE sample is slightly slower than that of the non-GBE sample, thus delaying the arrival of necking point in the GBE sample and improving the ductility of AL6XN super-ASS (Fig. 4c, d).

To sum up, the effect of GBE on the work hardening behavior of AL6XN super-ASS is schematically illustrated in Fig. 10. The GBE treatment reduces the work hardening rate of AL6XN super-ASS at the early stage of plastic deformation by weakening the back stress strengthening and dislocation increment; however, it can effectively improve the maintainable capacity of work hardening by weakening the pile-up of dislocations and inhibiting dislocation annihilation, thereby the uniformity of deformation and ductility are improved in GBE samples.

5 Conclusions

1. The GBE treatment has little effect on the yield strength, but slightly reduces the ultimate strength and improves the ductility of AL6XN super-ASS to a certain extent.

Such an influence of GBE on the tensile properties is closely related to the role of GBE playing in various work hardening stages.

2. At the early stage (Stages I and II) of plastic deformation, GBE raises the dislocation-free path, and reduces the back stress caused by GBs, thus inducing a slightly lowered work hardening rate; however, at the middle and latter stages (Stages III and IV), the work hardening rate of GBE samples gradually surpasses that of non-GBE samples due to the higher maintainable capacity of work hardening that is profited from an enhanced inhibition of dislocation annihilation.
3. The high fraction of SBs effectively channels the slip of dislocations in GBE samples, which enhances the deformation uniformity of AL6XN super-ASS and improves its maintainable capacity of work hardening. As a result, GBE postpones the appearance of necking point and efficaciously ameliorates the ductility.

Acknowledgements This work was financially supported by the National Natural Science Foundation of China (NSFC) under Grant Nos. 51871048 and 52171108. Special thanks to Mr. J.N. Deng, Y. Dong and Ms. N. Zhang in Analytical and Testing Center of Northeastern University for the assistance with TEM and EBSD characterizations.

Declarations

Conflicts of Interest The authors state that there are no conflicts of interest to disclose.

References

1. R.O. Ritchie, *Nat. Mater.* **10**, 817 (2011)
2. R.Z. Valiev, T.G. Langdon, *Prog. Mater. Sci.* **51**, 881 (2006)
3. M.A. Meyers, K.K. Chawla, *Mechanical behavior of materials* (Cambridge University Press, Cambridge, 2009)
4. D. Han, X.J. Guan, Y. Yan, F. Shi, X.W. Li, *Mater. Sci. Eng. A* **743**, 745 (2019)
5. R. Liu, Y.Z. Tian, Z.J. Zhang, P. Zhang, X.H. An, Z.F. Zhang, *Acta Mater.* **144**, 613 (2018)
6. J.Y. He, W.H. Liu, H. Wang, Y. Wu, X.J. Liu, T.G. Nieh, Z.P. Lu, *Acta Mater.* **62**, 105 (2014)
7. S. Qu, X.H. An, H.J. Yang, C.X. Huang, G. Yang, Q.S. Zang, Z.G. Wang, S.D. Wu, Z.F. Zhang, *Acta Mater.* **57**, 1586 (2009)
8. S. Qu, C.X. Huang, Y.L. Gao, G. Yang, S.D. Wu, Q.S. Zang, Z.F. Zhang, *Mater. Sci. Eng. A* **475**, 207 (2008)
9. N. Tsuchida, Y. Tomota, H. Moriya, O. Umezawa, K. Nagai, *Acta Mater.* **49**, 3029 (2001)
10. B.C. De Cooman, Y. Estrin, S.K. Kim, *Acta Mater.* **142**, 283 (2018)
11. S. Martin, C. Ullrich, D. Rafaja, *Mater. Today* **2**, S643 (2015)
12. Z. Zhuo, S. Xia, Q. Bai, B.X. Zhou, *J. Mater. Sci.* **53**, 2844 (2018)
13. X.J. Guan, F. Shi, H.M. Ji, X.W. Li, *Scr. Mater.* **187**, 216 (2020)
14. X.J. Guan, Z.P. Jia, S.M. Liang, F. Shi, X.W. Li, *J. Mater. Sci. Technol.* **113**, 82 (2022)
15. A. Telang, A.S. Gill, M. Kumar, S. Teyseyre, D. Qian, S.R. Manmana, V.K. Vasudevan, *Acta Mater.* **113**, 180 (2016)

16. X. Dong, N. Li, Y.A. Zhou, H.B. Peng, Y.T. Qu, Q. Sun, H.J. Shi, R. Li, S. Xu, J.Z. Yan, *J. Mater. Sci. Technol.* **93**, 244 (2021)
17. F. Shi, L. Yan, J. Hu, L.F. Wang, T.Z. Li, W. Li, X.J. Guan, C.M. Liu, X.W. Li, *Acta Metall. Sin. -Engl. Lett.* **35**, 1849 (2022)
18. C.M. Barr, A.C. Leff, R.W. Demott, R.D. Doherty, M.L. Taheri, *Acta Mater.* **144**, 281 (2018)
19. M. Kumar, W.E. King, A.J. Schwartz, *Acta Mater.* **48**, 2081 (2000)
20. X.J. Guan, F. Shi, H.M. Ji, X.W. Li, *Mater. Sci. Eng. A* **765**, 138299 (2019)
21. P.C. Zhao, B. Guan, Y.G. Tong, R.Z. Wang, X. Li, X.C. Zhang, S.T. Tu, *J. Mater. Sci. Technol.* **109**, 54 (2022)
22. Q.M. Wang, Y.J. Zhang, D. Han, X.W. Li, *Acta Metall. Sin. -Engl. Lett.* **35**, 651 (2022)
23. Z.Y. Wang, D. Han, X.W. Li, *Mater. Sci. Eng. A* **679**, 484 (2017)
24. D. Han, J.X. He, X.J. Guan, Y.J. Zhang, X.W. Li, *Metals* **9**, 151 (2019)
25. P. Chen, S.C. Mao, Y. Liu, F. Wang, Y.F. Zhang, Z. Zhang, X.D. Han, *Mater. Sci. Eng. A* **580**, 114 (2013)
26. S.S. Rui, Q.N. Han, X. Wang, S.L. Li, X.F. Ma, Y. Su, Z.P. Cai, D. Du, H.J. Shi, *Mater. Today. Commun.* **27**, 102445 (2021)
27. S.I. Wright, M.M. Nowell, D.P. Field, *Microsc. Microanal.* **17**, 316 (2011)
28. A.C. Leff, C.R. Weinberger, M.L. Taheri, *Ultramicroscopy* **153**, 9 (2015)
29. M. Calcagnotto, D. Ponge, E. Demir, D. Raabe, *Mater. Sci. Eng. A* **527**, 2738 (2010)
30. J. Kadkhodapour, S. Schmauder, D. Raabe, S. Ziaei-Rad, U. Weber, M. Calcagnotto, *Acta Mater.* **59**, 4387 (2011)
31. A. Kundu, D.P. Field, *Mater. Sci. Eng. A* **667**, 435 (2016)
32. M.F. Ashby, *Philos. Mag. A* **21**, 399 (1970)
33. Y.F. Wang, C.X. Huang, Q. He, F.J. Guo, M.S. Wang, L.Y. Song, Y.T. Zhu, *Scr. Mater.* **170**, 76 (2019)
34. X. Fang, Q.Q. Xue, K.Y. Yu, R.G. Li, D.Q. Jiang, L. Ge, Y. Ren, C.F. Chen, X.L. Wu, *Mater. Res. Lett.* **8**, 417 (2020)
35. S. Shukla, D. Choudhuri, T.H. Wang, K.M. Liu, R. Wheeler, S. Williams, B. Gwalani, R.S. Mishra, *Mater. Res. Lett.* **6**, 676 (2018)
36. S. Poulat, B. Décamps, L. Priester, *Philos. Mag. A* **77**, 1381 (1998)
37. N.V. Malyar, B. Grabowski, G. Dehm, C. Kirchlechner, *Acta Mater.* **161**, 412 (2018)
38. L. Lu, Y.F. Shen, X.H. Chen, L.H. Qian, K. Lu, *Science* **304**, 422 (2004)
39. D. Han, Z.Y. Wang, Y. Yan, F. Shi, X.W. Li, *Scr. Mater.* **133**, 59 (2017)
40. D. Han, Y.J. Zhang, X.W. Li, *Acta Mater.* **205**, 116559 (2021)
41. G.R. Leverant, M. Gell, S.W. Hopkins, *Mater. Sci. Eng. A* **8**, 125 (1971)
42. H. Mecking, U.F. Kocks, *Acta Metall.* **29**, 1865 (1981)
43. U.F. Kocks, H. Mecking, *Prog. Mater. Sci.* **48**, 171 (2003)
44. M. Murayama, K. Hono, H. Hirukawa, T. Ohmura, S. Matsuoka, *Scr. Mater.* **41**, 467 (1999)
45. M. Grujicic, X.W. Zhou, W.S. Owen, *Mater. Sci. Eng. A* **169**, 103 (1993)
46. C. Chen, F.C. Zhang, B. Lv, H. Ma, L. Wang, H.W. Zhang, W. Shen, *Mater. Sci. Eng. A* **761**, 138015 (2019)
47. X.L. Liu, Q.Q. Xue, W. Wang, L.L. Zhou, P. Jiang, H.S. Ma, F.P. Yuan, Y.G. Wei, X.L. Wu, *Materialia* **7**, 100376 (2019)
48. M.Y. Jiang, G. Monnet, B. Devincre, *J. Mech. Phys. Solids* **143**, 104071 (2020)
49. Z.W. Wang, Y.B. Wang, X.Z. Liao, Y.H. Zhao, E.J. Lavernia, Y.T. Zhu, Z. Horita, T.G. Langdon, *Scr. Mater.* **60**, 52 (2009)
50. H. Shao, D. Shan, K.X. Wang, G.J. Zhang, Y.Q. Zhao, *Results. Phys.* **15**, 102722 (2019)

Springer Nature or its licensor (e.g. a society or other partner) holds exclusive rights to this article under a publishing agreement with the author(s) or other rightsholder(s); author self-archiving of the accepted manuscript version of this article is solely governed by the terms of such publishing agreement and applicable law.